Egy. J. Pure & Appl. Sci. 2023; 61 (2):19-27

Egyptian Journal of Pure and Applied Science

Simulation study of zinc/cobalt doped methyl ammonium lead iodide for solar cells

Alaa E. Abd El-Samad [1, 2], Nasr Gad [1], Mostafa El-Aasser [1], Ahmed Mourtada Elseman [2]

[1] *Physics Department, Faculty of Science, Ain Shams University, Cairo 11566, Egypt*

[2] *Electronic & Magnetic Materials Department, Advanced Materials Institute, Central Metallurgical Research and Development Institute (CMRDI), Helwan, P.O. Box 87, Cairo 11421, Egypt*

ARTICLE INFO

Received 18 March 2023
Accepted 29 May 2023

Keywords
Perovskite solar cells,
Lead toxicity ,
Perovskite materials,
Photovoltaics.

Correspondence
Alaa Elshahat
E-mail*
(Corresponding Author)
alaaelshahat303@gmail.com

ABSTRACT

Lead-based Perovskite materials and solar cells attracted attention in the last decade, however, lead toxicity hinders the way to commercialization; therefore, partial, or total replacement of lead by environmentally friendly materials is suggested. In this work, wxAMPS software is employed to study the electrical characteristics of $MAPbI_3$, $MAPbZnI_3$, and $MAPbCoI_3$ as active layers in the cell configuration (FTO/ TiO_2/perovskite /Spiro-MeOTAD/Ag). The thickness of the different active layers is optimized from 200 nm – 800 nm for the best electrical performance. For $MAPbI_3$, the best electrical parameters of (24.54%, 23.41 mA/cm^2) is achieved at 550 nm thickness, while for $MAPb_{0.9}Zn_{0.1}I_3$ (23.96%, , 23,17 mA/cm^2) is obtained at 500 nm. $MAPb_{0.9}Co_{0.1}I_3$ achieves the highest PCE of 24.97% at 700 nm. With increasing the active layer thickness, PCE and short-circuit current increase; however, at the same time the fill factor and open-circuit voltage decrease. The quantum efficiency (QE) is also simulated at different thicknesses for the three active layers. QE of the cells with different active layers increases with the thickness. The QE in the wavelengths ranges from 600-800 nm increases from 71% at 200 nm to 89% at thicknesses 550, 500, and 700 nm for $MAPbI_3$, $MAPbZnI_3$, and $MAPbCoI_3$, respectively. The PCE is not only affected by the active layer thickness, but also by its defect density. The optimum defect density for the best PCE is obtained at 1x10^{14} cm^{-3}. This simulation study confirms that $MAPb_{0.9}Zn_{0.1}I_3$, and $MAPb_{0.9}Co_{0.1}I_3$, are promising materials for high-efficiency perovskite solar cells.

1. Introduction

Perovskite materials and solar cells have exceptional properties and numerous benefits. Organic-inorganic hybrid perovskite materials have received a lot of attention in the solar cell field because of their excellent photovoltaic properties like strong light absorption, good carrier mobility, long exciton lifetime and diffusion length, and solution processability.

In recent years, solar cells' efficiency based on these materials has risen from 3.8% to more than 25% [1,2]. Due to their straightforward structure and superior performance, perovskite cells are suitable as next-generation photovoltaic devices [3]. The formula for a 3D-perovskite structure is ABX_3 with methyl ammonium (MA) as the common A-site, lead (Pb) as the B-site, and X as a halogen ion such as I^-, Cl^-, Br^-. The methyl ammonium (MA) cation is primarily responsible for the structural stability of the perovskite film in the traditional perovskite $MAPbI_3$. As a result of the relatively weak interactions between MA cation and three-dimensional (3D) Pb-I framework, large-size organic ion MA can effectively stabilize this perovskite structure, while making little or no contribution to the electronic structure of $MAPbI_3$ near the band edge. At the same time, metal (Pb-site) has a considerable influence on electronic properties and significantly impacts the band gap of halide perovskite [4,5,6,7].

Lead (Pb) is a main element in perovskite materials. Nevertheless, its harmful environmental impact must be prevented or at least limited use [8,9]. Lead is the best choice for perovskite materials yet; because it has unique characteristics that make it qualified to harvest the best stability and efficiency. So, we can replace a percentage of it to maintain its advantages and improve them as well. Many research use elements as lead substitutes, such as tin, silver, and others [10,11,12,13]. Additives act as impurities that may provide Perovskite with more features and improve its performance. Tin (Sn) is a suitable element to replace Pb because Sn is located in group 14 with Pb and has an ionic radius of 0.94 A°, while Pb has an ionic radius of 1.2 A° [25]. So, different works discussed lead – tin-based perovskite with different percentages, structures, and techniques like in Hao et al., Lucia Serrano-Lujan et al., Jiaxing Song et al. and others [27,28,29,30], but Sn has a critical issue in terms of stability. So, different elements are used. In 2017, a new class of homo-valent metals was investigated as dopants in perovskite crystals. As a result of the similar atomic radii and the divalent nature, Pb^{+2} could be partially replaced by Co^{2+}, Zn^{2+}, Mg^{2+}, and Ni^{2+} [31].

After that, several large-scale studies on Zn^{2+} doping began. Zinc is particularly appealing due to its non-toxic properties, incapability to oxidize easily, and abundance on Earth. Doping with various Zn (II) percentages resulted in smoother films with fewer pinholes. Zn^{2+} interacts more strongly with the MA^+ cation and the I anion [32]. Cobalt is also a promising dopant, according to Matthew T. Klug and colleagues [36]. They concluded that the Pb: Co series exhibits several intriguing electronic and crystallographic properties while maintaining competitive photovoltaic performance at low levels of Pb substitution (3% molar).

By increasing the Voc over the baseline MAPbI3 while maintaining the FF and producing only a slightly reduced Jsc, a champion efficiency of 17.2% was achieved with an optimum molar ratio of 63Pb:1Co. Furthermore, XRD spectral crystallographic analysis reveals that increasing the Co2+ fraction at the lattice B-sites can controllably induce a cubic-to-tetragonal crystal structure transition. In this simulation work, different perovskite solar cells are simulated with different active layers. The thickness of the active layers is optimized to get the best electrical parameters. In addition, the defect density is optimized for all active layers. wxAMPS is the simulation tool used in this research.

2. Materials and methods

The materials used as active layers in these simulated solar cells are $MAPbI_3$, $MAPbZnI_3$, and $MAPbCoI_3$ with wxAMPS software as our tool in this theoretical study. wxAMPS is a 1D simulation program for solar cells that supports intra-band tunneling and trap-assisted tunneling models [14,15,16]. The simulation is based on the cell configuration of transparent conductive oxide (glass + FTO) as the transparent substrate, and perovskite material sandwiched between hole- blocking layer (TiO_2) and electron-blocking layer (Spiro-MeOTAD), finally the back contact (Ag). The cell's structure used here is shown in Fig. 1a. Further, Table 1 summarizes the main cell layer's parameters defined in the simulation. The band gap and the electron affinity had E_g and χ symbols, respectively. The relative permittivity parameter is simplified as ε_r, while μ_n and μ_p are defined as the electron and hole mobilities, respectively. The effective density of states for the conduction and valence band and the defect density are represented as N_c, N_v, and N_t, respectively. N_d and N_c donated to donor and acceptor density. The electron and hole thermal velocity is set to 10^7 cm/s, and the active layer's absorption data are extracted from ref. [37].

The simulated parameters were selected from different reported works [6,15,17,18,19,20,21,22]. The simulation is run with AM1.5G as the illumination condition and 27 °C as the default temperature.To obtain the electrical parameters of the perovskite cells, wxAMPS employs equations such as Poisson and continuity equations. These equations deal with charge, transportation, and density.

$$\frac{dy}{dx}\left(-\varepsilon(x)\frac{d\Psi}{dx}\right) = q\left[p(x) - n(x) + {N_d}^+(x) - {N_a}^-(x) + p_t(x) - n_t(x)\right] \quad (1)$$

where n and p represent the concentrations of free electrons and holes, respectively; n_t and p_t. represent the densities of trapped electrons and holes, respectively; and N_d^+ and N_a^-. represent the proportions of ionized donors and acceptors. q is the electron charge, Ψ is the electrostatic potential, and ε is the interfacial permittivity of the semiconductor.

The charge transport features, recombination rates, and generation rates are all included in the continuity equation, as shown by forms (2) and (3):

$$\frac{1}{q}\frac{dJn}{dx} = R_n(X) - G(X) \quad (2)$$

$$\frac{1}{q}\frac{dJp}{dx} = G(X) - R_p(X) \quad (3)$$

When R_n and R_p are the steady-state recombination velocities of electrons and holes, these forms describe the continuity equations. G denotes the optical generation rate, while J_n and J_p denote the electron and hole current densities. two types of recombination exist in these equations: intrinsic and extrinsic. When an electron from the conduction band lands in the valence band and recombines with a hole, recombination occurs in the intrinsic type.

This type of band-to-band recombination is known as direct recombination (R_d). Extrinsic recombination occurs at an intermediate state, which represents indirect recombination (R_i). As shown in the equation, R(x) is the sum of direct and indirect recombination (4)

$$R(x) = R_d(x)+R_i(x) \quad (4)$$

For getting the optical generation rate, we can use equation (5)

$$G(x) = -\frac{d}{dx}\sum \phi_i{}^{in}(\lambda_i) + \frac{d}{dx}\sum \phi_i{}^{ref}(\lambda_i) \quad (5)$$

where ϕi in and ϕi ref are the photon flux of the light incoming and reflected from the rear surface at a wavelength λ of i at some location x, depending on the light absorption coefficient and the light reflectance in the forward and reverse directions.

There is also recombination at the interfaces, this recombination velocity (S) [6] can be extracted by equation (6)

$$S_m = \frac{\int_{int} R\, dx}{m} \quad (6)$$

where R is the recombination rate within the interface layer, it stands for the whole interface layer, and m denotes the concentration of holes and electrons. The exact values of R and m are obtained from the numerical solution, and the integral of R across the whole interface layer represents the total interface recombination.

3. Factors upon which cell performance depends

There are many factors that affect solar cells' performance. The carrier transport layers' type, thickness, and defect density have a huge impact on the efficiency of the whole cell. On the other hand, the active layer has the most influence on the cell. So, in this section, we discussed the factors that affect the electrical parameters of solar cells such as the active layer thickness and defect density at the same parameters of the hole and electron transport layers.

3.1 The active layer thickness

The active layer is the most essential part of solar cells, and it is the layer responsible for providing carriers. Therefore, this layer must be chosen carefully.

The thickness of this layer is one of the factors that have an actual effect on the electrical parameter over the entire cell, as it must be proportional to the absorption coefficient and other factors. In this part, the thickness of the active layer is optimized to get the best efficiency. The influence of the absorber thickness on electrical device parameters was examined by varying the thickness of the absorbing layer in the range of 200 nm to 800 nm.

The IV- curves of the cell with different active layers are shown in Fig. 1(b, c, d). As appears in Fig. 1b, the best short-circuit current J_{sc} (23.81 mA/cm^2) is achieved at a thickness of 800 nm, and the highest open-circuit voltage V_{oc} (1.459 V) is observed for 200 nm for $MAPbI_3$. While the IV- characteristics for $MAPb_{0.9}Zn_{0.1}I_3$ can be seen in Fig. 1c, and the best J_{sc} (23.7 mA/cm^2) and V_{oc} (1.439 V) is achieved at thickness 800 nm and 200 nm, respectively. The highest J_{sc} (23.811 mA/cm^2) and V_{oc} (1.479 V) are also achieved for $MAPb_{0.9}Co_{0.1}I_3$ at thicknesses 800 nm and 200 nm, respectively, as shown in Fig. 1d. So, we can notice that our simulated cells achieved the best J_{sc} with higher thickness in contrast to V_{oc} which achieved the best results in thin layers.

Fig. 2 shows how the active layer thickness affects the electrical parameters. In Fig. 2a $MAPbCoI_3$ achieved the best efficiency along the different thicknesses against $MAPbI_3$ and $MAPb_{0.9}Zn_{0.1}I_3$. The cell harvests higher efficiency with increasing thickness for the three active layers, but at a certain thickness, it started decreasing again. For $MAPbI_3$, the highest efficiency was obtained at a thickness of 550 nm, but for $MAPb_{0.9}Zn_{0.1}I_3$ the best efficiency was obtained at a thickness of 500 nm. At 700 nm, the highest efficiency of 24.97% is achieved using $MAPb_{0.9}Co_{0.1}I_3$ as the active layer. As the absorbing layer's thickness increases, the material absorbs lighter, resulting in more photons, which increase the generation of electron and hole pairs, resulting in improved device efficiency [23,24], but after a certain thickness, the thickness becomes longer than the diffusion length. As a result, recombination increases. Simultaneously, V_{oc} is reduced by increasing the thickness. Fig. 2b shows that increased recombination in the thicker absorber layer results in a lower V_{oc}.

$$V_{oc} = \frac{nkT}{q}\ln\left(\frac{I_l}{I_o} + 1\right) \quad (V)$$

From the previous equation (V), V_{oc} depends on the dark generation and saturation currents ratio. Where n is the ideality factor, (kT/q) is the thermal voltage, I_l is light generated current, and Io is the dark saturation current [25,26]. In Fig. 2c, the J_{sc}-efficiency curve of $MAPbI_3$, $MAPb_{0.9}Zn_{0.1}I_3$, and $MAPb_{0.9}Co_{0.1}I_3$ appears. As mentioned before, when the thickness increase, more light can be absorbed, and more carrier concentration are created, which brings J_{sc} values to elevate.

Since perovskite material has a very high absorption coefficient, normally up to 10^5 cm^{-1}, the cell can obtain very high values of J_{sc} and PCE. As V_{oc}, the fill factor (FF) parameter decreases with the thickness, as shown in Fig. 2d. The reason for this is that the electric field has a strong influence on the fill factor, and the electric field in the absorber decreases as the forward bias increases. It will result in less carrier collection, which the electric field will aid. [34, 35]. Fig. 3 exhibits the effect of the active layer thickness on the quantum efficiency (QE). For $MAPbI_3$ and $MAPb_{0.9}Zn_{0.1}I_3$, QE boosted from 71% to 88.8% at the wavelength range from 600 – 800 nm, as shown in Fig. 3(a, b). for $MAPb_{0.9}Co_{0.1}I_3$, QE boosted from 71.2% to 89% at the area of the wavelength from 600 – 800 nm, as shown in Fig. 3c.

3.2 The active layer's defect density

The cell's electrical parameter is not only affected by the active layer thickness but also by the density of defects. So, the defect density of the active layer is optimized to select the best value. The density of defects varied from 10^{14} cm^{-3} to 10^{18} cm^{-3}, and it is clear to what extent it affected the electrical performance as appears in Fig. 3. In Fig. 4a the defect density with V_{oc} is shown and as can be seen, when increasing the defect density, V_{oc} decrease from 1.4 v, 1.39 v, and 1.41v at 1x 10^{14} cm^{-3} to 1.27, 1.25, and 1.2 at 1x10^{18} cm^{-3} for $MAPbI_3$, $MAPb_{0.9}Zn_{0.1}I_3$, and $MAPb_{0.9}Co_{0.1}I_3$, respectively.

The efficiency also falls for all cells with increasing defect density, as shown in Fig. 4b. In Fig. 4c, decreasing in J_{sc} with increasing defect density is observed. In Fig. 4d, also a decrease in FF with increasing defect density is observed. We can note that all the cell performance is negatively affected by increasing the defect density and the power conversion efficiency parameter is the most affected. The increase in the defect density leads to an increase in recombination resulting in a drop in the electrical parameters. In the previous section, the carrier recombination is also increased.

Nevertheless, the increased thickness helped in increasing the amount of the absorbed light, so J_{sc}, and efficiency increased. In other words, when the increase in absorbing light is more than the increase in recombination, enhancement in electrical parameters can be observed. But in this case, the defect density increased so the recombination increased and there is no way to reserve the electrical parameters. So, as expected a drop in the whole electrical parameters occurred. Table 2 summarizes the electrical parameters at the optimized thickness and defect density.

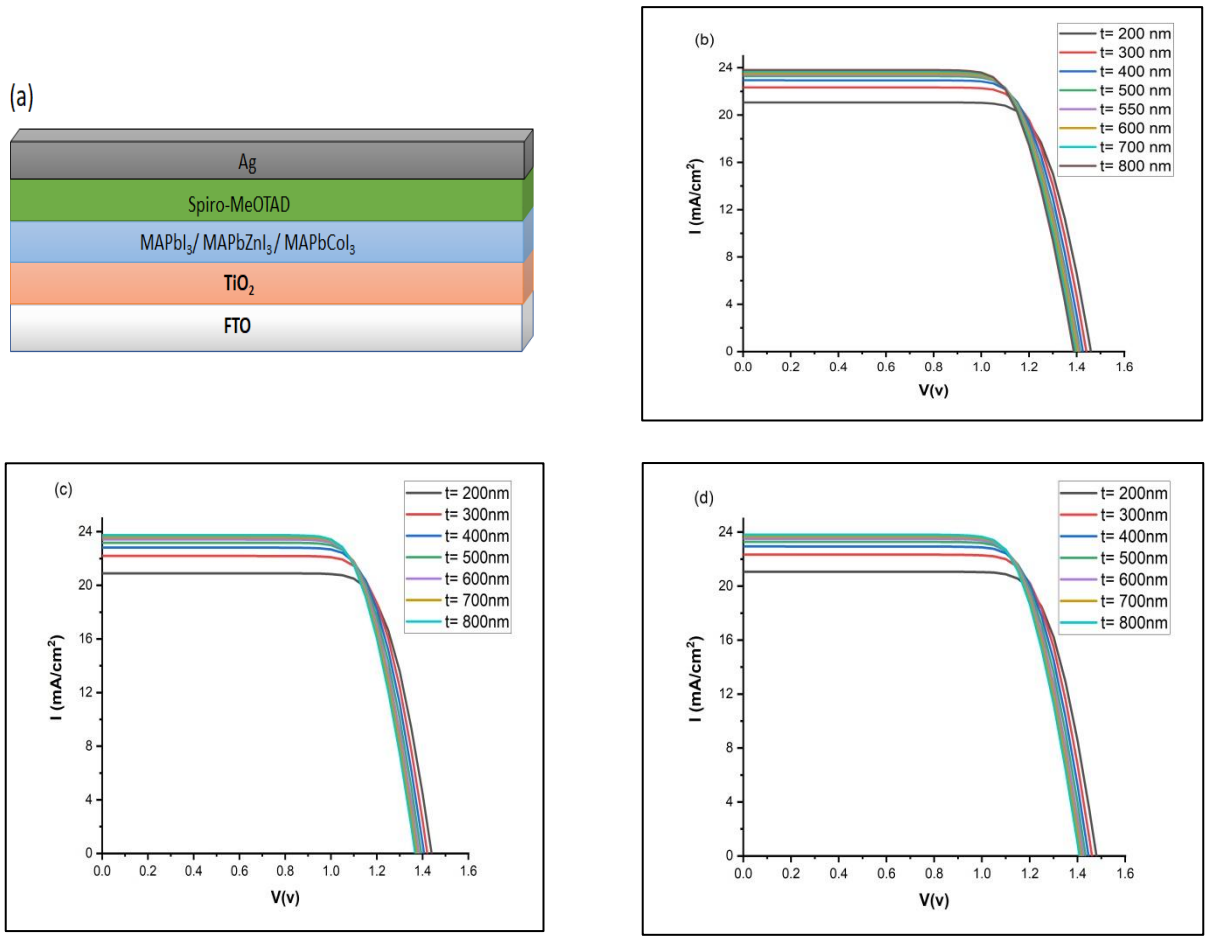

Fig. 1 (a) Perovskite solar cell's general structure, **(b)** the IV curve of $MAPbI_3$ at different thicknesses, **(c)** the IV curve of $MAPbznI_3$ at different thicknesses, and **(d)** the IV curve of $MAPbCoI_3$ at different thicknesses.

Table 1. The simulation parameters

parameters	TiO_2	$MAPbI_3$	$MAPbZnI_3$	$MAPbCoI_3$	Spiro-MeOTAD
Thickness (nm)	200	200-800	200-800	200-800	300
permittivity	100	10	10	10	3
E_g (ev)	3.2	1.54	1.52	1.56	2.91
χ (ev)	4	3.93	3.93	3.93	2.05
Nc (cm^{-3})	$2x10^{18}$	$2.8 x10^{18}$	$2.8 x10^{18}$	$2.8 x10^{18}$	$2.2 x10^{18}$
Nv (cm^{-3})	$1.8 x10^{19}$	$3.9 x10^{18}$	$3.9 x10^{18}$	$3.9 x10^{18}$	$1.8 x10^{19}$
μ_n (cm^2/v/s)	20	15	15	15	$1 x10^{-4}$
μ_p (cm^2/v/s)	10	15	15	15	$1 x10^{-4}$
N_d	$1 x10^{17}$	$1 x10^{9}$	$1 x10^{9}$	$1 x10^{9}$	0
N_a	0	$1 x10^{9}$	$1 x10^{9}$	$1 x10^{9}$	$4 x10^{17}$
Energy level	1.1	1.2	1.2	1.2	1.1
Capture N	$1 x10^{-19}$	$1 x10^{-20}$	$1 x10^{-20}$	$1 x10^{-20}$	$1 x10^{-19}$
Capture P	$1 x10^{-18}$	$1 x10^{-19}$	$1 x10^{-19}$	$1 x10^{-19}$	$1 x10^{-18}$
Defect density	$1 x10^{17}$	variable	variable	variable	$1 x10^{17}$

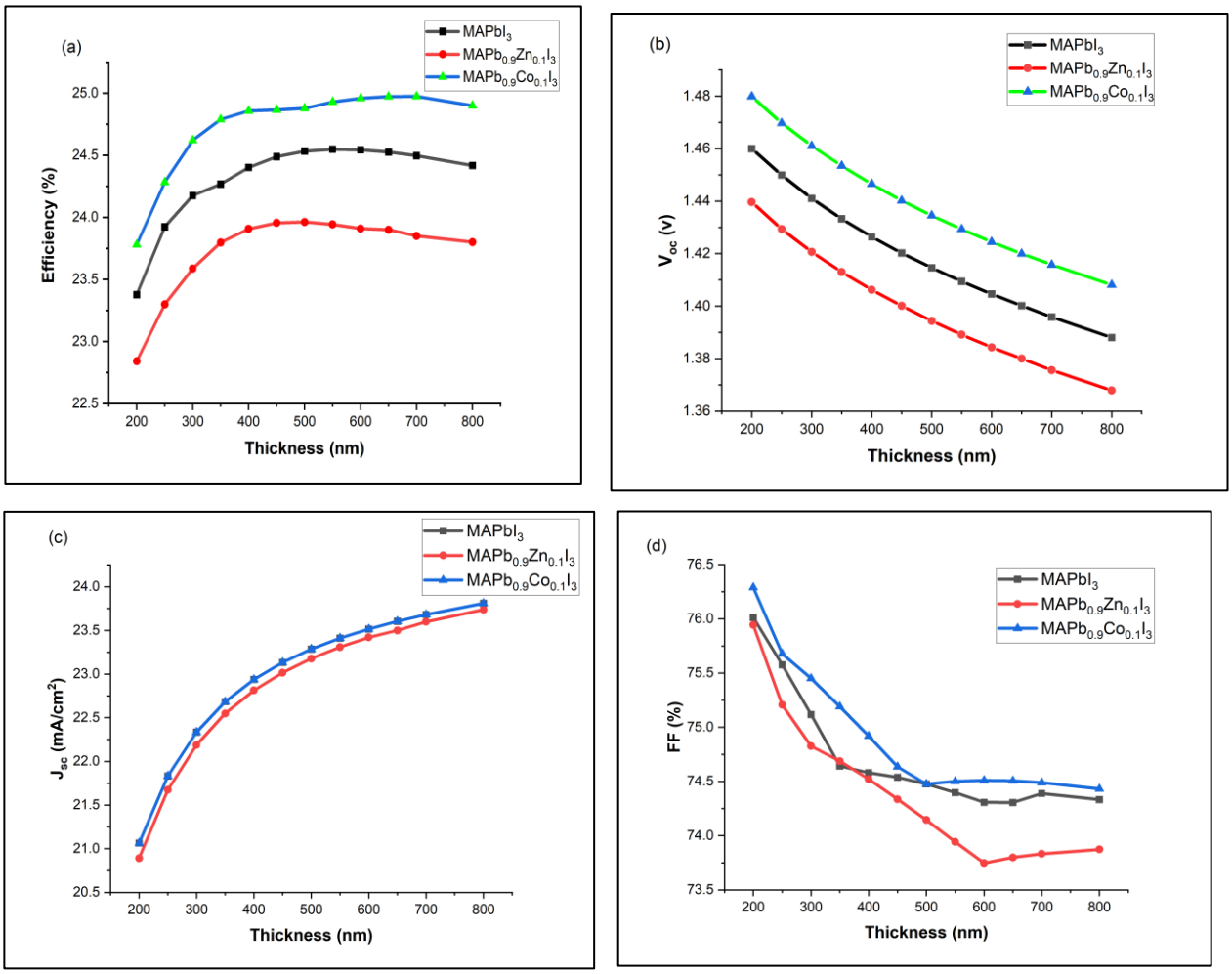

Fig. 2 The relation between the thickness and **(a)** efficiency, **(b**) open-circuit voltage (Voc), **(c)** short-circuit current (Jsc), and **(d)** fill factor (FF).

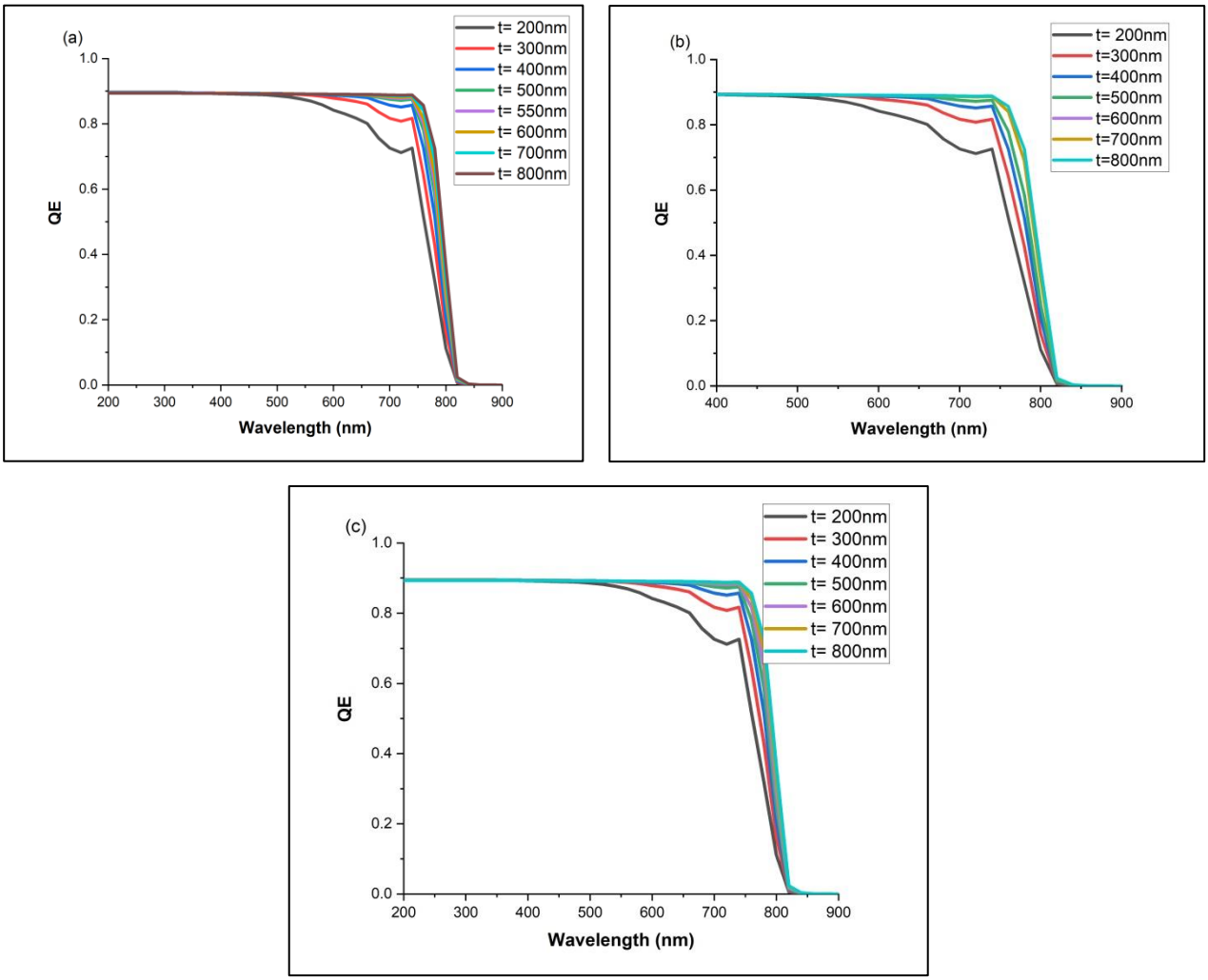

Fig. 3 (a) The relation between wavelength and QE at different thicknesses, **(a)** QE of $MAPbI_3$, **(b)** QE of $MAPb_{0.9}Zn_{0.1}I_3$, and **(c)** QE of $MAPb_{0.9}Co_{0.1}I_3$.

Table 2. The effect of defect density on the electrical parameters for the proposed perovskite solar cells at the optimum thickness

Perovskite material	V_{oc} (v)	J_{sc} (mA/cm^2)	FF	PCE (%)	Defect density (cm^{-3})
$MAPbI_3$	1.409429	23.41067	74.39746	24.54795	1 x 10^{14}
$MAPb_{0.9}Zn_{0.1}I_3$	1.394401	23.17707	74.14519	23.96235	1 x 10^{14}
$MAPb_{0.9}Co_{0.1}I_3$	1.415779	23.6815	74.48976	24.97475	1 x 10^{14}

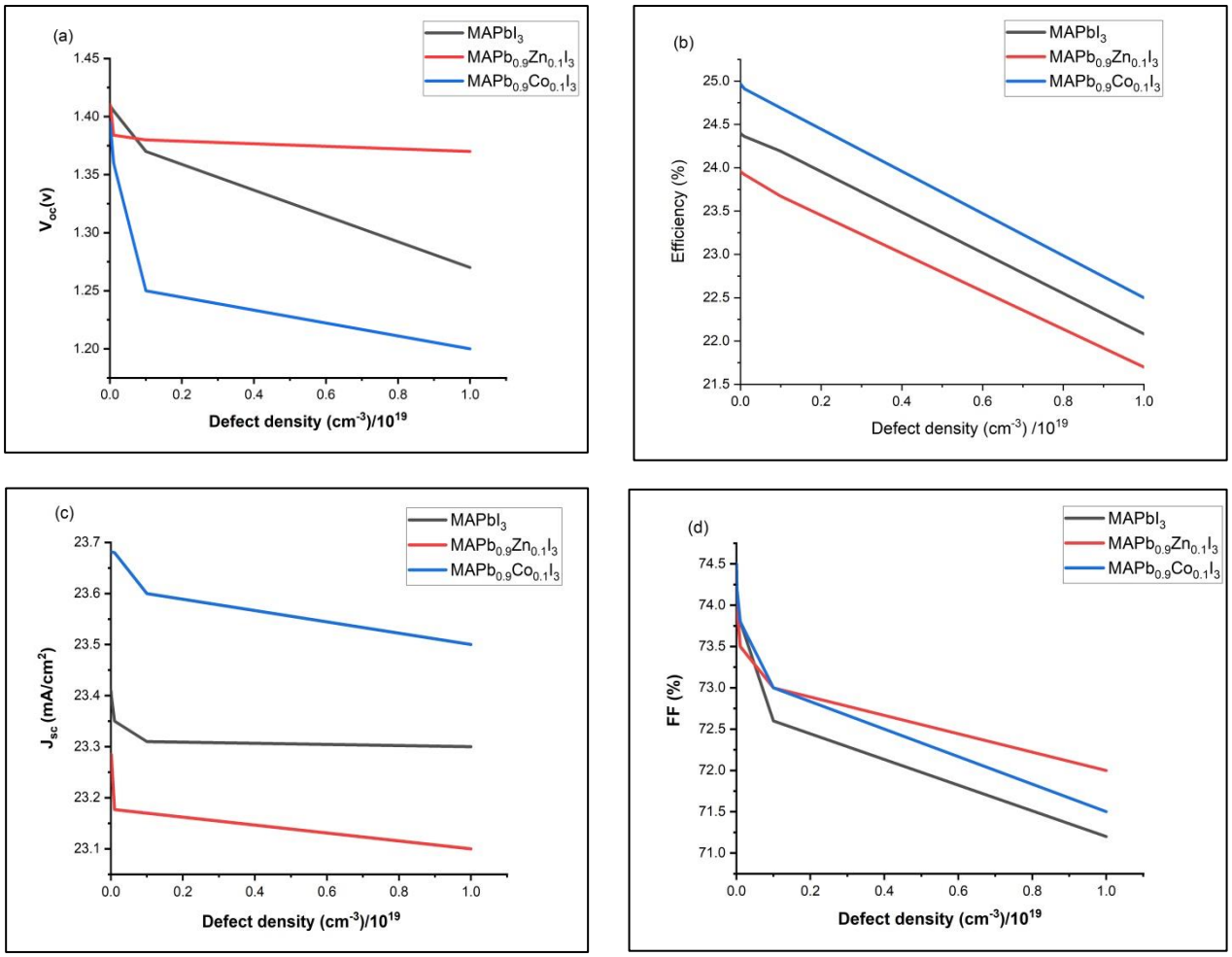

Fig. 4 The relation between the total defect density of $MAPbI_3$, $MAPb_{0.9}Zn_{0.1}I_3$, and $MAPb_{0.9}Co_{0.1}I_3$ and **(a)** V_{oc}, **(b)** efficiency, **(c)** J_{sc}, **(d)** FF.

4. Conclusion

Perovskite solar cells are simulated using wxAMPS software. $MAPbI_3$ and $MAPb_{0.9}Zn_{0.1}I_3$, and $MAPb_{0.9}Co_{0.1}I_3$ perovskite materials are employed in the simulation as active layers. Thier thickness is optimized and the best performance appears at thicknesses of 550 nm, 500 nm, and 700 nm for $MAPbI_3$ and $MAPb_{0.9}Zn_{0.1}I_3$, and $MAPb_{0.9}Co_{0.1}I_3$, respectively. The best efficiency and short-circuit current (24.97%, 23.68 mA/cm^2) was obtained using cobalt doped lead perovskite layer, followed by pure lead perovskite (24.5%, 23.41 mA/cm^2). QE is also enhanced at the last thicknesses and boosted from 71% up to 89%. Defect density is also studied for the modeling of perovskite solar cells, and the highest electrical parameters are achieved at the minimum defect density value of $1x10^{14}$ cm^{-3}.

5. Reference

1. **Heo, J. H., Im, S. H., Noh, J. H., Mandal, T. N., Lim, C. S., Chang, J. A., ... & Seok, S. I. (2013).** Efficient inorganic–organic hybrid heterojunction solar cells containing perovskite compound and polymeric hole conductors. Nature photonics, **7(6), 486-491.**
2. **Bouazizi, S., Tlili, W., Bouich, A., Soucase, B. M., & Omri, A. (2022).** Design and efficiency enhancement of FTO/PC60BM/CsSn0. 5Ge0. 5I3/Spiro-OMeTAD/Au perovskite solar cell utilizing SCAPS-1D Simulator. Materials Research Express, **9(9), 096402.**

3. **Jin, J., Li, H., Chen, C., Zhang, B., Xu, L., Dong, B., ... & Dai, Q. (2017).** Enhanced performance of perovskite solar cells with zinc chloride additives. ACS applied materials & interfaces, **9(49), 42875-42882.**
4. **Conings, B., Drijkoningen, J., Gauquelin, N., Babayigit, A., D'Haen, J., D'Olieslaeger, L., ... & Boyen, H. G. (2015).** Intrinsic thermal instability of methylammonium lead trihalide perovskite. Advanced Energy Materials, **5(15), 1500477.**
5. **Niu, G., Yu, H., Li, J., Wang, D., & Wang, L. (2016).** Controlled orientation of perovskite films through mixed cations toward high performance perovskite solar cells. Nano Energy, **27, 87-94.**
6. **Guerrero, A., Juarez-Perez, E. J., Bisquert, J., Mora-Sero, I., & Garcia-Belmonte, G. (2014).** Electrical field profile and doping in planar lead halide perovskite solar cells. Applied Physics Letters, **105(13), 133902.**
7. **Yin, W. J., Shi, T., & Yan, Y. (2014).** Unusual defect physics in CH3NH3PbI3 perovskite solar cell absorber. Applied Physics Letters, **104(6), 063903.**
8. **Kumar, N., & Narayanasamy, S. (2022).** Toxicological assessment and adsorptive removal of lead (Pb) and Congo red (CR) from water by synthesized iron oxide/activated carbon (Fe3O4/AC) nanocomposite. Chemosphere, **294, 133758.**
9. **Cuomo, D., Foster, M. J., & Threadgill, D. (2022).** Systemic review of genetic and epigenetic factors underlying differential toxicity to environmental lead (Pb) exposure. Environmental Science and Pollution Research, **1-16.**
10. **Fatema, K., & Arefin, M. S. (2022).** Enhancing the efficiency of Pb-based and Sn-based perovskite solar cell by applying different ETL and HTL using SCAPS-ID. Optical Materials, **125, 112036.**
11. **Jha, K. K., Tripathy, S. K., Laref, A., & Lenka, T. R. (2022, April).** Comparative Study of Ge-doped CH 3 NH 3 Ge x Pb (1-x) I 3 Perovskite Solar Cell By SCAPS-1D Software. In 2022 IEEE International Conference on Nanoelectronics, Nanophotonics, Nanomaterials, Nanobioscience & Nanotechnology (5NANO) **(pp. 1-6).** IEEE.
12. **Chen, Q., Chen, L., Ye, F., Zhao, T., Tang, F., Rajagopal, A., ... & Chen, L. (2017).** Ag-incorporated organic–inorganic perovskite films and planar heterojunction solar cells. Nano letters, **17(5), 3231-3237.**
13. **Eze, V. O., Carani, L. B., Majumder, H., Uddin, M. J., & Okoli, O. I. (2022).** Inorganic cesium lead mixed halide based perovskite solar materials modified with functional silver iodide. Scientific reports, **12(1), 1-10.**
14. **Elseman, A., Shalan, A., Rashad, M., Hassan, A., 2017.** Experimental and simulation study for impact of different halides on the performance of planar perovskite solar cells. Materials Science in Semiconductor Processing **66, 176-185.**
15. **Liu, Y., Sun, Y., Rockett, A., (2012).** A new simulation software of solar cells—wxAMPS. Solar Energy Materials and Solar Cells **98, 124-128.**
16. **Sajid, S., Elseman, A.M., Ji, J., Dou, S., Wei, D., Huang, H., Cui, P., Xi, W., Chu, L., Li, Y., (2018).** Computational study of ternary devices: stable, low-cost, and efficient planar perovskite solar cells. Nano-micro letters **10(3), 1-11.**
17. **Azri, F., Meftah, A., Sengouga, N., Meftah, A., (2019).** Electron and hole transport layers optimization by numerical simulation of a perovskite solar cell. Solar energy **181, 372-378.**
18. **Elseman, A., Ji, J., Dou, S., Huang, H., Cui, P., Wei, D., Li, M., (2018).** Novel hole transport layer of nickel oxide composite with carbon for high-performance perovskite solar cells. Chinese Physics B **27(1), 017305.**
19. **Husainat, A., Ali, W., Cofie, P., Attia, J., Fuller, J., (2019).** Simulation and analysis of methylammonium lead iodide (CH3NH3PbI3) perovskite solar cell with Au contact using SCAPS 1D simulator. American Journal of Optics and Photonics **7(2), 33.**
20. **Sajid, S., Elseman, A.M., Ji, J., Dou, S., Wei, D., Huang, H., Cui, P., Xi, W., Chu, L., Li, Y., (2018).** Computational study of ternary devices: stable, low-cost, and efficient planar perovskite solar cells. Nano-micro letters **10(3), 1-11.**

21. **Sultana, N.A., Islam, M.O., Mahmood, Z.H., (2017).** Utilization of low cost metals as back contact with Perovskite Solar Cell. Dhaka Univ J Appl Sci Eng **4, 35-38.**
22. **Jahan, S., Tasnuva, R., & Matin, M. A. (2021, December).** Improving the efficiency and stability of Perovskite-CdTe tandem solar cell: A numerical simulation study with wx-AMPS. In 2021 6th International Conference on Development in Renewable Energy Technology (ICDRET) **(pp. 01-06).** IEEE.
23. **Et-taya, L., Ouslimane, T., & Benami, A. (2020).** Numerical analysis of earth-abundant Cu2ZnSn (SxSe1-x) 4 solar cells based on Spectroscopic Ellipsometry results by using SCAPS-1D. Solar Energy, **201, 827-835.**
24. **Rai, S., Pandey, B. K., & Dwivedi, D. K. (2020).** Modeling of highly efficient and low cost CH3NH3Pb (I1-xClx) 3 based perovskite solar cell by numerical simulation. Optical Materials, **100, 109631.**
25. **Liu, X., Yang, Z., Chueh, C. C., Rajagopal, A., Williams, S. T., Sun, Y., & Jen, A. K. Y. (2016).** Improved efficiency and stability of Pb–Sn binary perovskite solar cells by Cs substitution. Journal of Materials Chemistry A, **4(46), 17939-17945.**
26. **Zhu, Z., Li, N., Zhao, D., Wang, L., & Jen, A. K. Y. (2019).** Improved efficiency and stability of Pb/Sn binary perovskite solar cells fabricated by galvanic displacement reaction. Advanced Energy Materials, **9(7), 1802774.**
27. **Hao, F., Stoumpos, C. C., Chang, R. P., & Kanatzidis, M. G. (2014).** Anomalous band gap behavior in mixed Sn and Pb perovskites enables broadening of absorption spectrum in solar cells. Journal of the American Chemical Society, **136(22), 8094-8099.**
28. **Serrano-Lujan, L., Espinosa, N., Larsen-Olsen, T. T., Abad, J., Urbina, A., & Krebs, F. C. (2015).** Tin-and lead-based perovskite solar cells under scrutiny: an environmental perspective. Advanced Energy Materials, **5(20), 1501119.**
29. **Gu, S., Lin, R., Han, Q., Gao, Y., Tan, H., & Zhu, J. (2020).** Tin and mixed lead–tin halide perovskite solar cells: progress and their application in tandem solar cells. Advanced Materials, **32(27), 1907392.**
30. **Song, J., Hu, W., Li, Z., Wang, X. F., & Tian, W. (2020).** A double hole-transport layer strategy toward efficient mixed tin-lead iodide perovskite solar cell. Solar Energy Materials and Solar Cells, **207, 110351.**
31. **Klug, M. T., Osherov, A., Haghighirad, A. A., Stranks, S. D., Brown, P. R., Bai, S., ... & Belcher, A. M. (2017).** Tailoring metal halide perovskites through metal substitution: influence on photovoltaic and material properties. Energy & Environmental Science, **10(1), 236-246.**
32. **Kooijman, A., Muscarella, L. A., & Williams, R. M. (2019).** Perovskite thin film materials stabilized and enhanced by zinc (II) doping. Applied Sciences, **9(8), 1678.**
33. **Burger, S., Ehrenreich, M. G., & Kieslich, G. (2018).** Tolerance factors of hybrid organic–inorganic perovskites: recent improvements and current state of research. Journal of Materials Chemistry A, **6(44), 21785-21793.**
34. **Tan, K., Lin, P., Wang, G., Liu, Y., Xu, Z., & Lin, Y. (2016).** Controllable design of solid-state perovskite solar cells by SCAPS device simulation. Solid-State Electronics, **126, 75-80.**
35. **Mandadapu, U., Vedanayakam, S. V., & Thyagarajan, K. (2017).** Simulation and analysis of lead based perovskite solar cell using SCAPS-1D. Indian J. Sci. Technol., **10(11), 65-72.**
36. **Klug, M. T., Osherov, A., Haghighirad, A. A., Stranks, S. D., Brown, P. R., Bai, S., ... & Belcher, A. M. (2017).** Tailoring metal halide perovskites through metal substitution: influence on photovoltaic and material properties. Energy & Environmental Science, **10(1), 236-246.**
37. **Abd El-Samad, A. E., Gad, N., El-Aasser, M., Rashad, M. M., & Elseman, A. M. (2022).** Optoelectronic investigation and simulation study of zinc and cobalt doped lead halide perovskite nanocrystals. Solar Energy, **247, 553-563.**